Phase diagram of the Kane-Mele-Coulomb model

M. Hohenadler,[1] F. Parisen Toldin,[1] I. F. Herbut,[2] and F. F. Assaad[1]

[1]*Institut für Theoretische Physik und Astrophysik, Universität Würzburg, Am Hubland, 97074 Würzburg, Germany*
[2]*Department of Physics, Simon Fraser University, Burnaby, British Columbia, Canada V5A 1S6*

We determine the phase diagram of the Kane-Mele model with a long-range Coulomb interaction using an exact quantum Monte Carlo method. Long-range interactions are expected to play a role in honeycomb materials because the vanishing density of states in the semimetallic weak-coupling phase suppresses screening. According to our results, the Kane-Mele-Coulomb model supports the same phases as the Kane-Mele-Hubbard model. The nonlocal part of the interaction promotes short-range sublattice charge fluctuations, which compete with antiferromagnetic order driven by the onsite repulsion. Consequently, the critical interaction for the magnetic transition is significantly larger than for the purely local Hubbard repulsion. Our numerical data are consistent with SU(2) Gross-Neveu universality for the semimetal to antiferromagnet transition, and with 3D XY universality for the quantum spin Hall to antiferromagnet transition.

I. INTRODUCTION

Inspired by the experimental realization of graphene [1], electrons with a linear band dispersion, or Dirac fermions, have become a major topic in condensed matter physics. Interest in correlated fermions on the honeycomb lattice has been boosted by the theoretical proposal of the quantum spin Hall (QSH) state [2], debates about the existence of a topological Mott insulator [3–6] and a quantum spin-liquid phase [7–11], and the mean-field prediction of an interaction-generated topological phase (the QSH* phase) in a model for Na_2IrO_3 [12,13].

In order to make analytical and numerical studies feasible, previous work has often invoked the approximation of a purely local (Hubbard) repulsion between electrons [14]. The honeycomb Hubbard model can be simulated using exact quantum Monte Carlo methods [7,15,16], and has received considerable interest after reports of a gapped spin-liquid phase at intermediate interactions [7]. Simulations can also be carried out for the Hubbard model with additional spin-orbit coupling [17,18], usually referred to as the Kane-Mele-Hubbard (KMH) model [19], which provides a framework to study correlated topological insulators in two dimensions [20].

The existence of Dirac cones at isolated points in the Brillouin zone, as compared to a Fermi surface, is a key feature of the honeycomb lattice [21]. In the absence of interactions and for a half-filled band, the system is a semimetal (SM) with the density of states vanishing at the Fermi level [22]. The SM is stable at weak coupling [23], and any phase transitions take place at finite critical interactions. According to analytical calculations, the universality of the Mott-Hubbard transition should be modified by the presence of gapless fermionic modes [10,23–25]. The vanishing of the density of states also implies that the Coulomb interaction will not be screened, and that the approximation of a Hubbard interaction is therefore *a priori* not justified. The long-range Coulomb interaction leads to a logarithmic divergence of the Fermi velocity [26,27] which was confirmed experimentally [28], and marginal Fermi-liquid behavior [27]. On the other hand, the divergence of the velocity makes the long-range interaction in graphene marginally irrelevant at the critical point in the framework of the ϵ expansion [24]. This result for weak

interactions, which holds close to $3+1$ dimensions [23,24,27] as well as close to $1+1$ dimension [29], suggests the same universality class for the Mott transition as in the Hubbard model.

For the Hubbard model, our present understanding based on numerical and analytical results suggests the existence of a second-order Mott transition from a semimetallic to an antiferromagnetic phase at $U/t \approx 3.8$, with no intermediate spin-liquid phase [9,10]. The KMH model with additional spin-orbit coupling instead undergoes a transition from a quantum spin Hall (QSH) state to an antiferromagnetic phase, also at a finite critical U [17–19]. The phase diagram is shown in Fig. 2(b). Quantum Monte Carlo (QMC) data are consistent with the predicted SU(2) Heisenberg Gross-Neveu universality for the Hubbard model [10], and with three-dimensional (3D) XY universality for the KMH model [30]. The honeycomb lattice with long-range Coulomb interaction has been investigated in detail in the context of graphene (see [21] for a review). An interaction-driven metal-insulator transition in graphene was demonstrated using quantum Monte Carlo simulations [31]. More recently, long-range Coulomb interaction has been studied in models with Dirac and Weyl fermions [32–35], including the KM model [33].

In this work, we present exact results for electrons on the honeycomb lattice interacting via a $1/r$ Coulomb potential. The auxiliary-field QMC method used is free of a sign problem at half-filling, and can be applied to more general nonlocal interactions. Here, we study the phase diagram of the Kane-Mele-Coulomb model. In the absence of spin-orbit coupling, we find a quantum phase transition from a SM to an antiferromagnet consistent with the Gross-Neveu universality class, with the critical point shifted to larger interaction strengths compared to the Hubbard model. At a nonzero spin-orbit coupling, the KM model with long-range electron-electron interaction is found to be either in a QSH or in a magnetic insulating state. Similar to the KMH model, the phase transition is consistent with the 3D XY universality class, but again occurs at larger values of the interaction. We find no evidence of a potential, intermediate QSH* phase [13] or any other additional phases.

The paper is organized as follows. In Sec. II, we define the models. Section III provides a discussion of the QMC method. Our results are presented in Sec. IV, and Sec. V contains our conclusions.

II. KANE-MELE-COULOMB MODEL

The KM Hamiltonian [2,36] can be written as

$$\hat{H}_0 = -t \sum_{\langle i,j \rangle} \hat{c}_i^\dagger \hat{c}_j + i\lambda \sum_{\langle\langle i,j \rangle\rangle} \hat{c}_i^\dagger (\boldsymbol{v}_{ij} \cdot \boldsymbol{\sigma}) \hat{c}_j. \quad (1)$$

Here, we have used the spinor notation $\hat{c}_i^\dagger = (c_{i\uparrow}^\dagger, c_{i\downarrow}^\dagger)$, where $c_{i\sigma}^\dagger$ creates an electron with spin σ at site $\boldsymbol{i}$. The symbols $\langle \boldsymbol{i,j} \rangle$ and $\langle\langle \boldsymbol{i,j} \rangle\rangle$ denote pairs of nearest-neighbor and next-nearest-neighbor lattice sites on the honeycomb lattice, respectively, and implicitly include the Hermitian conjugate terms. The first term corresponds to the usual nearest-neighbor hopping [21]. The second term describes the z component of Rashba spin-orbit coupling [36] in graphene, which takes the form of a complex next-nearest-neighbor hopping $\pm i\lambda$. The sign depends on the sublattice, the electron spin, and the direction of the hopping process. It may be compactly written in the form $\boldsymbol{v}_{ij} \cdot \boldsymbol{\sigma}$, with

$$\boldsymbol{v}_{ij} = \frac{\boldsymbol{d}_{ik} \times \boldsymbol{d}_{kj}}{|\boldsymbol{d}_{ik} \times \boldsymbol{d}_{kj}|}. \quad (2)$$

The vector $\boldsymbol{d}_{ik}$ (with vanishing z component) connects sites $\boldsymbol{i}$ and $\boldsymbol{k}$, $\boldsymbol{k}$ being the intermediate lattice site between $\boldsymbol{i}$ and $\boldsymbol{j}$; $\boldsymbol{\sigma} = (\sigma^x, \sigma^y, \sigma^z)$ is the Pauli vector.

The QMC method used here can be applied to a rather general electron-electron interaction of the form

$$\hat{H}_V = \frac{1}{4} \sum_{ij} V_{ij}(\hat{n}_i - 1)(\hat{n}_j - 1), \quad (3)$$

with a positive-definite matrix V. The numerical results shown were obtained for the specific choice

$$V_{ij} = \begin{cases} 2U, & \text{if } |\boldsymbol{i} - \boldsymbol{j}| = 0 \\ \frac{\alpha U \delta}{|\boldsymbol{i}-\boldsymbol{j}|}, & \text{if } |\boldsymbol{i} - \boldsymbol{j}| > 0. \end{cases} \quad (4)$$

In Eq. (4), α determines the relative strength of the onsite and the nonlocal interactions, and $\delta = \frac{2}{3}|\boldsymbol{a}_2 - \frac{1}{2}\boldsymbol{a}_1|$ is the distance between the two orbitals in the unit cell [$\boldsymbol{a}_1 = (1,0)$, $\boldsymbol{a}_2 = \frac{1}{2}(1,\sqrt{3})$ are the basis vectors of the honeycomb lattice]. The distance $|\boldsymbol{i} - \boldsymbol{j}|$ is the minimal distance between the sites $\boldsymbol{i}$ and $\boldsymbol{j}$. For $\alpha = 0$, $\hat{H}_V$ reduces to the Hubbard interaction

$$\hat{H}_U = \frac{U}{2} \sum_i (\hat{n}_i - 1)^2. \quad (5)$$

We refer to the Hamiltonian $\hat{H} = \hat{H}_0 + \hat{H}_V$, with V_{ij} defined as in Eq. (4) as the *Kane-Mele-Coulomb* (KMC) model. Its Hamiltonian respects C_3 rotational symmetry, U(1) spin symmetry, Z_2 time-reversal symmetry, and U(1) gauge invariance. In the absence of spin-orbit coupling ($\lambda = 0$), we recover the full C_6 rotation symmetry of the lattice, and SU(2) spin symmetry. At half-filling, there is an additional particle-hole symmetry.

Throughout the paper we will consider half-filled lattices with $L \times L$ unit cells and periodic boundary conditions. The number of lattice sites is given by $N = 2L^2$.

III. QUANTUM MONTE CARLO METHOD

We discuss the method for a Hamiltonian $\hat{H} = \hat{H}_0 + \hat{H}_V$, with $\hat{H}_0$ given by Eq. (1) and a general, nonlocal interaction as defined by Eq. (3).

The starting point for the implementation of the long-range interaction is the action

$$S(\{A,c^\dagger,c\}) = S_0(\{c^\dagger,c\}) + \int_0^\beta d\tau \sum_i iA(\boldsymbol{i},\tau)[n_{i\sigma}(\tau) - 1]$$

$$+ \int_0^\beta d\tau \sum_{ij} A(\boldsymbol{i},\tau) V_{ij}^{-1} A(\boldsymbol{j},\tau). \quad (6)$$

Here, S_0 corresponds to the action of the noninteracting Hamiltonian (1), $n_i(\tau) = \sum_\sigma c_{i\sigma}^\dagger(\tau) c_{i\sigma}(\tau)$, and $A(\boldsymbol{i},\tau)$ is a real scalar field. If the matrix V_{ij} is positive definite, the Gaussian integral over the scalar field can be carried out to give

$$S(\{c^\dagger,c\}) = S_0(\{c^\dagger,c\}) + S_1(\{c^\dagger,c\}) \quad (7)$$

with

$$S_1(\{c^\dagger,c\}) = \frac{1}{4} \int_0^\beta d\tau \sum_{ij} [n_i(\tau) - 1] V_{ij} [n_j(\tau) - 1]. \quad (8)$$

A similar approach was used in Ref. [37].

The action in the presence of the scalar field is quadratic in the fermionic degrees of freedom. The latter can hence be integrated out to obtain

$$S(\{A\}) = \int_0^\beta d\tau \sum_{ij} A(\boldsymbol{i},\tau) V_{ij}^{-1} A(\boldsymbol{j},\tau)$$

$$- \ln \text{Tr}[\mathcal{T} e^{-\int_0^\beta d\tau \hat{H}(\{A\})}], \quad (9)$$

where

$$\hat{H}(\{A\}) = \hat{H}_0 + \sum_i iA(\boldsymbol{i},\tau)(\hat{n}_i - 1). \quad (10)$$

The presence of particle-hole and U(1) spin symmetry guarantees that the action is real. In particular, the U(1) spin symmetry allows us to factorize the trace into spin-up and spin-down contributions

$$\text{Tr}[\mathcal{T} e^{-\int_0^\beta d\tau \hat{H}(\{A\})}] = \prod_\sigma \text{Tr}_\sigma[\mathcal{T} e^{-\int_0^\beta d\tau \hat{H}_\sigma(\{A\})}]. \quad (11)$$

With the canonical transformation $c_{i\uparrow}^\dagger \rightarrow (-)^i c_{i\downarrow}$, where $(-)^i$ takes the value 1 (-1) on the A (B) sublattice, we can show that (the bar denotes complex conjugation)

$$\text{Tr}_\uparrow[\mathcal{T} e^{-\int_0^\beta d\tau \hat{H}_\uparrow(\{A\})}] = \overline{\text{Tr}_\downarrow[\mathcal{T} e^{-\int_0^\beta d\tau \hat{H}_\downarrow(\{A\})}]}. \quad (12)$$

Therefore, the action $S(\{A\})$ is real and the weight for a given field configuration $e^{-S(\{A\})}$ is positive. Consequently, the Monte Carlo sampling of the scalar field does not suffer from the minus sign problem.

The implementation of the method relies on a Trotter discretization of imaginary time $\beta = L_\tau \Delta\tau$. There are many

possibilities for carrying out the sampling. A possible choice is hybrid molecular dynamics [31,37,38] based on a Gaussian integral representation of the determinant. Here, we have implemented a simpler, sequential updating scheme in which field configurations are proposed according to the probability $e^{\int_0^\beta d\tau \sum_{i,j} A(i,\tau) V_{ij}^{-1} A(j,\tau)}$ and then accepted or rejected using importance sampling. This approach is advantageous when the matrix V has a small number of low-lying eigenvalues that favor specific modulations of the scalar field. To implement the algorithm, we chose a basis where V is diagonal. Because V is symmetric and positive definite, we can find an orthogonal transformation M such that $M^\dagger V M = \text{diag}(\xi_1, \ldots, \xi_N)$ with $\xi_i > 0$. With $\Phi(i,\tau) = \sum_j M_{ij}^\dagger A(j,\tau)$, the partition function reads as

$$Z = \int D\{\Phi\} \prod_{i,\tau} e^{-\Delta\tau \Phi^2(i,\tau)/\xi_i} W(\{\Phi\}) + \mathcal{O}(\Delta\tau^2), \quad (13)$$

where

$$W(\{\Phi\}) = \text{Tr} \prod_\tau e^{-\frac{\Delta\tau}{2}\hat{H}_0} e^{-\Delta\tau \sum_{ij} i M_{ij} \Phi(j,\tau)(\hat{n}_i - 1)} e^{-\frac{\Delta\tau}{2}\hat{H}_0}. \quad (14)$$

We propose new configurations according to

$$T_0(\{\Phi\} \rightarrow \{\Phi'\}) = \prod_{i,\tau}\{P_{i\tau} P_0[\Phi'(i,\tau)] + (1 - P_{i\tau})\delta[\Phi_0(i,\tau)$$
$$- \Phi_0'(i,\tau)]\}, \quad (15)$$

with $P_0(\Phi'(i,\tau)) = \sqrt{\frac{\Delta\tau}{\pi\xi_i}} e^{-\Delta\tau \Phi'^2(i,\tau)/\xi_i}$. The proposed configuration $\{\Phi'\}$ is accepted with probability

$$P = \min\left(\frac{T_0(\{\Phi'\} \rightarrow \{\Phi\}) W_{\text{tot}}(\{\Phi'\})}{T_0(\{\Phi\} \rightarrow \{\Phi'\}) W_{\text{tot}}(\{\Phi\})}, 1\right)$$
$$\equiv \min\left(\frac{W(\{\Phi'\})}{W(\{\Phi\})}, 1\right). \quad (16)$$

Here, the total weight of a configuration is given by

$$W_{\text{tot}}(\{\Phi\}) = \prod_{i,\tau} P_0(\Phi(i,\tau)) W(\{\Phi\}). \quad (17)$$

The probabilities $P_{i,\tau}$ in Eq. (15) can be chosen arbitrarily, allowing us to optimize the acceptance rate. We have opted for a sequential updating of the time slices. We set $P_{i,\tau} \equiv P$ and used values of P that yield a good acceptance rate for updates.

Because we are interested in ground-state properties, we used the projective (zero-temperature) auxiliary-field QMC algorithm. Taking $|\Psi_T\rangle$ to be the ground state of the noninteracting Hamiltonian $\hat{H}_0$, and assuming that it has a finite overlap with the ground state $|\Psi_0\rangle$ of $\hat{H}$, expectation values can be calculated as

$$\frac{\langle\Psi_0|\hat{O}|\Psi_0\rangle}{\langle\Psi_0|\Psi_0\rangle} = \lim_{\Theta\to\infty} \frac{\langle\Psi_T|e^{-\Theta\hat{H}/2}\hat{O}e^{-\Theta\hat{H}/2}|\Psi_T\rangle}{\langle\Psi_T|e^{-\Theta\hat{H}}|\Psi_T\rangle}. \quad (18)$$

The implementation of the projective algorithm is similar to that for finite temperatures, a detailed description of which can be found in Ref. [39]. Dynamical correlation functions were computed with the method of Ref. [40]. We used a symmetric Trotter decomposition to minimize the systematic error, with $\Delta\tau t = 0.1$. A projection parameter $\Theta t = 40$ was sufficient
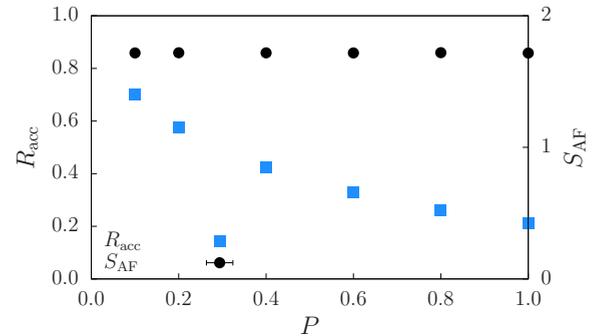
FIG. 1. (Color online) Acceptance rate R_{acc} for Monte Carlo updates and spin structure factor S_{AF} [Eq. (20)] as a function of the parameter P. Here, $U/t = 4$, $\alpha = 1$, $L = 6$.

to achieve convergence to the ground state within statistical errors.

Figure 1 shows the acceptance rate R_{acc} and the spin structure factor [Eq. (26)] as a function of the parameter P for $U/t = 4$ and $\alpha = 1$. The results reveal that P can be used to tune the acceptance rate without changing the values of physical observables.

Compared to the Hubbard interaction, simulations with the long-range interaction (4) and local updates become increasingly difficult at strong interactions, leading to long autocorrelation times. Because the phase transitions in the KMC model occur at larger interactions, the quality of the data and the finite-size extrapolations is not as good as for the KMH model [7,10,17,30].

IV. RESULTS

To better orient the discussion, we first present the phase diagram of the KMC model. Then, we discuss how the phase boundaries were obtained from finite-size scaling, look at the critical behavior, provide an explanation for the shift of the magnetic transition compared to the KMH model, and comment on the absence of new phases. We focus on $\alpha = 1$, but very similar results were obtained for $\alpha = 1.23$.

A. Phase diagram

The zero-temperature phase diagram of the KMC model with $\alpha = 1$, as obtained from QMC simulations, is shown in Fig. 2(a). For comparison, we also show the phase diagram of the KMH model in Fig. 2(b). As discussed in detail below, the phase boundaries are based on a finite-size scaling of the magnetization m. The data for the KMH model were taken from Refs. [10,17,30,41]. The restriction of the SM to $\lambda = 0$ follows from the fact that the spin-orbit term immediately opens a mass gap in a gapless Dirac metal, as previously illustrated for the KMH model [30].

Similar to the KMH model [7], the KMC model has a semimetallic ground state for $\lambda = 0$ and $U < U_c$; note that with our definition of the interaction in Eq. (4), both the local and the nonlocal parts of the interaction scale with U. For stronger interactions $U > U_c$, the ground state is an antiferromagnetic Mott insulator (MI). At nonzero spin-orbit coupling λ, we find a QSH phase up to a critical U_c, and

(a) Kane-Mele-Coulomb model

(b) Kane-Mele-Hubbard model
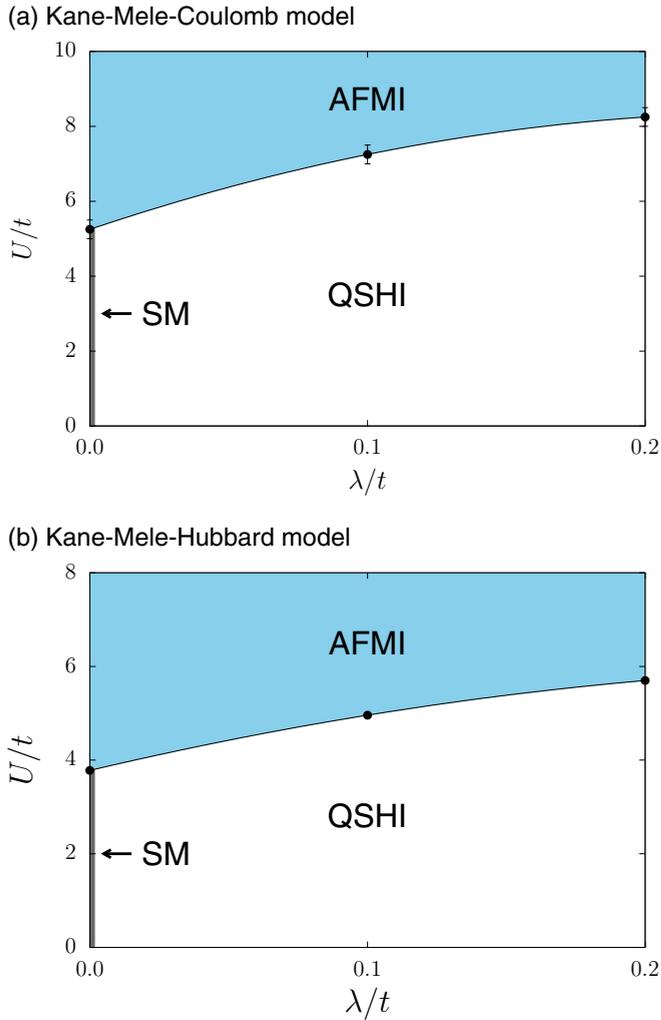
FIG. 2. (Color online) (a) Phase diagram of the KMC model with $\alpha = 1$. The phases correspond to a semimetal (SM) which exists for $\lambda = 0$, a quantum spin Hall insulator (QSHI), and an antiferromagnetic Mott insulator (AFMI). (b) Phase diagram of the KMH model (corresponding to $\alpha = 0$) based on previous simulations [10,17,30,41] (see also Ref. [42]).

again a magnetic insulator for $U > U_c$. The same phases have previously been observed in the KMH model [17–19] [see Fig. 2(b)]. As for the KMH model, the critical value for the transition increases with increasing λ. We have found no evidence for a previously reported quantum spin-liquid phase at intermediate interactions [7,17,30], consistent with recent numerical results for the Hubbard model [9–11].

As observed before for the KMH model, the magnetic ordering in the AFMI occurs in the transverse and longitudinal spin directions at $\lambda = 0$, whereas only the transverse spin components order at $\lambda > 0$. For the KMH model, the effective spin model [19] valid at large U/t contains exchange interactions $J = 4t^2/U$ and $J' = \pm 4\lambda^2/U$. The sign of J' is different for the z ($J' > 0$) and the xy ($J' < 0$) directions of spin. Because J and J' act between nearest- and next-nearest-neighbor spins, respectively, the z component becomes frustrated for $\lambda \neq 0$, favoring easy-plane antiferromagnetic order. The different symmetry of the order parameter at $\lambda = 0$

and $\lambda > 0$, and the absence or presence of gapless fermionic modes below U_c, also implies different universality classes for the corresponding phase transitions. Numerical results for the KMH model are consistent with an SU(2) Gross-Neveu transition for $\lambda = 0$ [10], and a U(1) 3D XY transition for $\lambda > 0$ [30].

B. Magnetic phase transition at $\lambda = 0$

The quantum phase transition from the SM to the AFMI in the Hubbard model on the honeycomb lattice ($\alpha = 0$, $\lambda = 0$) has attracted a lot of interest, partly because the transition has a finite critical value U_c, and can be studied exactly using QMC methods. An intriguing question is if the transition between these phases is a direct transition [9–11] or involves an intermediate spin-liquid phase [7,8]. After initial evidence for the existence of such a phase [7], more recent results on larger lattices [9] and using alternative methods to compute the order parameter [10] favor the scenario of a direct quantum phase transition. The absence of a jump in the double occupation (which corresponds to the derivative of the free energy with respect to U) at the critical point suggests that the transition is continuous [7].

In Ref. [10], it was shown that QMC results for the Mott transition of the honeycomb Hubbard model are consistent with a novel fermionic critical point described by the Gross-Neveu-Yukawa theory [24,43]. The latter describes Dirac fermions coupled to magnetic (bosonic) degrees of freedom via a Yukawa term [24]. The question we address here is if the nature of the transition is altered by a long-ranged Coulomb interaction. Analytically, it is possible to include the Coulomb potential with the help of a scalar field and show that it is, if weak, a (marginally) irrelevant perturbation [24].

To study the onset of long-range antiferromagnetic order, we consider the spin-spin correlation function

$$S_{\alpha\beta}(\boldsymbol{i} - \boldsymbol{j}) = \langle \boldsymbol{S}_i \cdot \boldsymbol{S}_j \rangle, \qquad (19)$$

where α (β) is the orbital index belonging to site $\boldsymbol{i}$ ($\boldsymbol{j}$), and the corresponding $\boldsymbol{Q} = 0$ structure factor

$$S_{\text{AF}} = \frac{1}{L^2} \sum_\alpha \sum_{ij} S_{\alpha\alpha}(\boldsymbol{i} - \boldsymbol{j}), \qquad (20)$$

where we have taken the trace over the orbitals. The magnetization per site is then given by

$$m = \sqrt{S_{\text{AF}}/N}. \qquad (21)$$

It extrapolates to zero in the nonmagnetic SM phase, but takes on a finite value in the thermodynamic limit for $U \geqslant U_c$, where U_c is the critical value for the magnetic phase transition. In contrast to previous work [10], we did not use pinning fields.

Figure 3(a) shows the finite-size scaling of the magnetization for different values of U/t. We simulated system sizes ranging from $L = 6$ to 18, and used quadratic fits for the extrapolation. Within the accuracy of this scaling procedure, the phase transition seems to occur between $U/t = 5$ and 5.5. The critical value is hence significantly larger than for the transition in the Hubbard model where $U_c/t = 3.78(5)$ [10].

As for the Hubbard model [10], we test if our data are compatible with the critical exponents $z = 1$, $\beta/\nu = 0.9$,
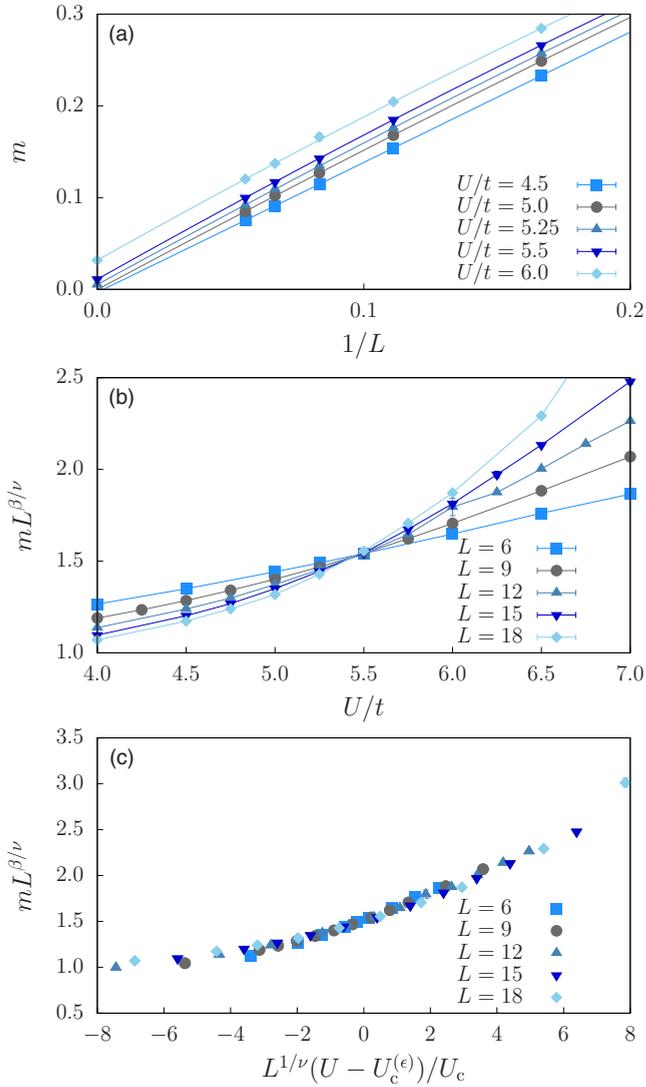
FIG. 3. (Color online) SM-AFMI quantum phase transition. (a) Finite-size scaling of the magnetization m using quadratic fits. (b) Scaling intersection using the critical exponents for the Gross-Neveu universality class from the ϵ expansion [10,24]. (c) Scaling collapse using the critical value $U_c^{(\epsilon)}/t = 5.45$. Here, $\lambda = 0$, $\alpha = 1$.

FIG. 4. (Color online) (a) Finite-size scaling of the single-particle gap using quadratic fits. (b) Expectation value of the interaction term, corresponding to the derivative of the free energy with respect to U. Here, $\lambda = 0$, $\alpha = 1$.

and $\nu = 1/2 + 21/55 \approx 0.88$ for the SU(2) Gross-Neveu universality class in 2+1 dimensions, obtained from the ϵ expansion with $\epsilon = 1$. The plot of $mL^{\beta/\nu}$ in Fig. 3(b) produces a satisfactory intersection of curves for different system sizes at a critical value $U_c^{(\epsilon)}/t = 5.45(10)$.

Using $U_c^{(\epsilon)}/t = 5.45$, we plot $mL^{\beta/\nu}$ as a function of $L^{1/\nu}(U - U_c)/U_c$ in Fig. 3(c). The rather good scaling collapse suggests that our numerical data are consistent with the Gross-Neveu critical exponents from the ϵ expansion, similar to the analogous transition in the Hubbard model [10]. The scaling collapse quickly deteriorates upon variation of $U_c^{(\epsilon)}$.

Figure 4(a) shows a finite-size scaling of the single-particle excitation gap Δ_{sp}, which is extracted from fits to the single-particle Green's function at the Dirac point, $G(\boldsymbol{q} = \boldsymbol{K}, \tau)$ [7,30]. Second-order polynomial extrapolations to the thermodynamic limit suggest a vanishing of the gap for

$U/t \leqslant 4.5$, and a very small but nonzero single-particle gap for $U/t \geqslant 5.5$. For $U/t = 5$, the data curve downward at large L; a quadratic fit suggests a small but nonzero gap.

The uncertainty in the finite-size extrapolation of m and Δ_{sp} is larger than for the KMH model. In particular, these quantities suggest a critical value in the range $[5,5.5]$, smaller than $U_c^{(\epsilon)}/t = 5.45(10)$ obtained using the critical exponents from the ϵ expansion. Apart from the limitations in system size, which affect the accuracy of the finite-size extrapolation of m and Δ_{sp}, it was previously shown that a measurement of m^2 instead of m is problematic close to the critical point [10]. In addition, we see evidence for logarithmic corrections to scaling for the system sizes considered. The critical value $U_c^{(\epsilon)}/t = 5.45(10)$ further depends on the ratio β/ν, with β and ν obtained from the ϵ expansion. The accuracy of the values for the critical exponents is unknown for the present model, but a recent comparison with QMC simulations for Z_2 and U(1) Gross-Neveu models showed good agreement [44,45]. A scaling analysis independent of critical exponents is beyond the scope of this paper, and will be published elsewhere.

Finally, Fig. 4(b) shows the free-energy derivative $\partial F/\partial U = \langle \hat{H}_V \rangle / U$ [see also Eq. (4)]. The continuous evolution of this quantity across the critical point suggests a continuous (second-order) phase transition.

C. Competition of spin and charge order

The main difference between the phase diagrams of the KMC and the KMH models is a shift of the magnetic phase
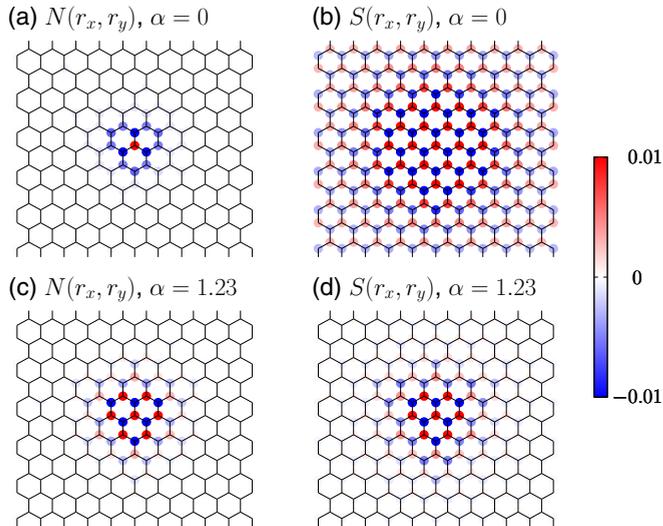
FIG. 5. (Color online) Real-space charge and spin correlations relative to the central site for (a), (b) the Hubbard model ($\alpha = 0$), and (c), (d) a long-range interaction ($\alpha = 1.23$). Here, $\lambda = 0$, $U/t = 3.5$, $L = 15$.

to larger values of U. For $\lambda = 0$, this shift can be understood already at the classical level where the total energy is given by

$$E_{\mathrm{cl}} = \frac{1}{4} \sum_{ij} (n_i - 1) V_{ij} (n_j - 1). \quad (22)$$

The state with uniform density at half-filling (that is, with $n_i = 1$) has $E_{\mathrm{cl}} = 0$. If V_{ij} is positive definite, all other charge configurations have a positive and hence higher energy. However, with increasing α, the energy of the charge-density-wave state with doubly occupied sites on sublattice A and empty sites on sublattice B (or vice versa) decreases, leading to a competition with the uniform state. For a model with onsite (U) and nearest-neighbor (V) repulsion only, the two states become degenerate when $3V = U$, whereas for the long-range interaction (4) degeneracy occurs close to $\alpha = 1.23$. The competition between the magnetic Mott state and the charge-density-wave state provides an explanation for the observed increase of the critical value U_c upon going from a Hubbard to a long-range interaction (see Fig. 2). The suppression of magnetic order can also be understood as resulting from a reduction of the effective onsite repulsion by the nonlocal interactions [46].

To illustrate this competition, we show in Fig. 5 the real-space charge-charge correlation function

$$N(\boldsymbol{r}) = \langle \hat{n}_{\boldsymbol{r}} \hat{n}_{\boldsymbol{0}} \rangle - \langle \hat{n}_{\boldsymbol{r}} \rangle \langle \hat{n}_{\boldsymbol{0}} \rangle, \quad (23)$$

and the spin-spin correlation function

$$S(\boldsymbol{r}) = \langle \hat{\boldsymbol{S}}_{\boldsymbol{r}} \cdot \hat{\boldsymbol{S}}_{\boldsymbol{0}} \rangle. \quad (24)$$

The results are for $\lambda = 0$ and $U < U_c$, corresponding to the semimetallic phase. For $\alpha = 0$ (Hubbard interaction), $N(\boldsymbol{r})$ is slightly suppressed around the origin with respect to the noninteracting system. This is typical of a liquid phase with contact interactions where charges avoid each other at short distances.

In the case of a long-range interaction, $\alpha = 1.23$, we find enhanced short-range charge correlations. At the same time, on going from $\alpha = 0$ to 1.23, we observe a significant suppression of spin correlations. These numerical data highlight the competition between charge and spin order, and hence support the explanation of the shift of U_c in terms of competing orders. Interestingly, even for $\alpha = 1.23$, where charge and spin correlations are nearly degenerate in the classical limit, we do not find a stable charge-ordered phase, but a direct transition from the SM to the AFMI phase.

D. Magnetic phase transition at $\lambda/t = 0.2$

Similar to the KMH model [19,30], the presence of spin-orbit coupling is expected to allow long-range magnetic order only in the transverse spin direction. To determine the phase boundary, we therefore measure the transverse spin correlation function[1]

$$S^{\pm}_{\alpha\beta}(\boldsymbol{i} - \boldsymbol{j}) = \langle S_i^+ S_j^- + S_i^- S_j^+ \rangle \quad (25)$$

from which we obtain the structure factor

$$S^{xy}_{\mathrm{AF}} = \frac{1}{L^2} \sum_{\alpha} \sum_{i,j} S^{\pm}_{\alpha\alpha}(\boldsymbol{i} - \boldsymbol{j}) \quad (26)$$

and the transverse magnetization

$$m_{xy} = \sqrt{S^{xy}_{\mathrm{AF}}/N}. \quad (27)$$

Figure 6(a) shows a finite-size scaling of m_{xy} for different values of U/t for the KMC model with $\alpha = 1$. The fits of the data to second-order polynomials suggest that the critical point is located in the range $U_c/t \in [8, 8.5]$, compared to the value $U_c/t = 5.70(3)$ found for the KMH model at the same spin-orbit coupling $\lambda/t = 0.2$. The enhanced critical value compared to the Hubbard case can again be attributed to the competition between charge and spin correlations (see Sec. IV C). Similar to the KMH model [30], we find no magnetic order in the spin-z direction over the whole range of interactions considered.

We can further test if the assumption of 3D XY universality, as previously demonstrated for the analogous transition in the KMH model [30], is consistent with our numerical data. Figure 6(b) shows the quantity $L^{\beta/\nu} m_{xy}$ as a function of U for different system sizes, taking the critical exponents $z = 1$, $\nu = 0.6717(1)$, and $\beta = 0.3486(1)$ of the 3D XY model [47]. We find an intersection of curves for different system sizes at a value of $U_c/t = 8.4(1)$, compatible with Fig. 6(a). In contrast to $\lambda = 0$, we do not observe logarithmic corrections to scaling as a result of the long-range interaction. Nevertheless, the large critical value of the transition renders simulations on large systems very demanding.

Taking $U_c/t = 8.4$, we can produce a satisfactory scaling collapse in Fig. 6(c). The consistency between the onset of the magnetization and the scaling intersection and collapse using the critical exponents of the 3D XY model suggests that the universality class of the transition is not changed by

---

[1]For the SU(2) symmetric case ($\lambda = 0$), we have the relation $S_{\alpha\beta}(\boldsymbol{i} - \boldsymbol{j}) = (3/4)S^{\pm}_{\alpha\beta}(\boldsymbol{i} - \boldsymbol{j})$.
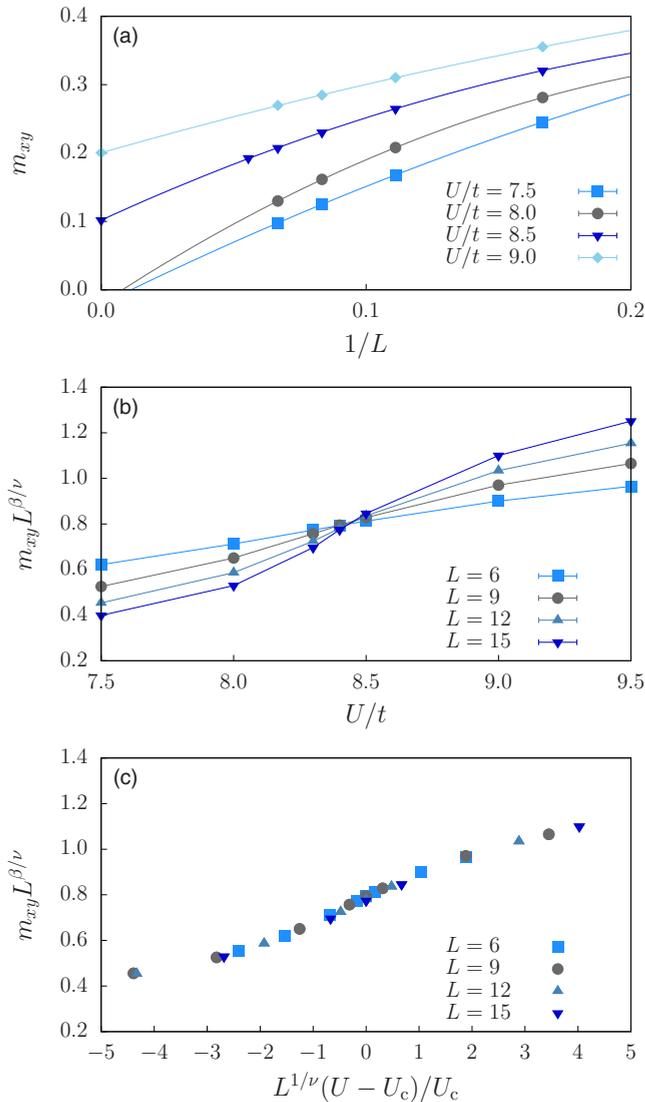
FIG. 6. (Color online) QSHI-AFMI quantum phase transition. (a) Finite-size scaling of the magnetization m_{xy} using quadratic fits. (b) Scaling intersection using the critical exponents of the 3D XY model [30,47]. (c) Scaling collapse using $U_c/t = 8.4$. Here, $\lambda/t = 0.2$, $\alpha = 1$.

the long-range interaction. In particular, the quality of the intersection and the data collapse in Fig. 6 are very similar to that for the KMH model [30]. We attribute the insensitivity to the nonlocal part of the interaction to the fact that the magnetic excitons (corresponding to particle-hole pairs) involved in the transition are charge neutral, and therefore not affected by modifications of the potential.

E. Absence of an intermediate phase

The shift of the phase boundary for the magnetic phase transition in the KMC model to significantly larger values of U/t provides room for the QSH* phase predicted to emerge from the interplay of strong spin-orbit coupling and strong electron-electron interaction in Na_2IrO_3 [13]. In particular, the QSH phase undergoes a transition to the QSH* phase
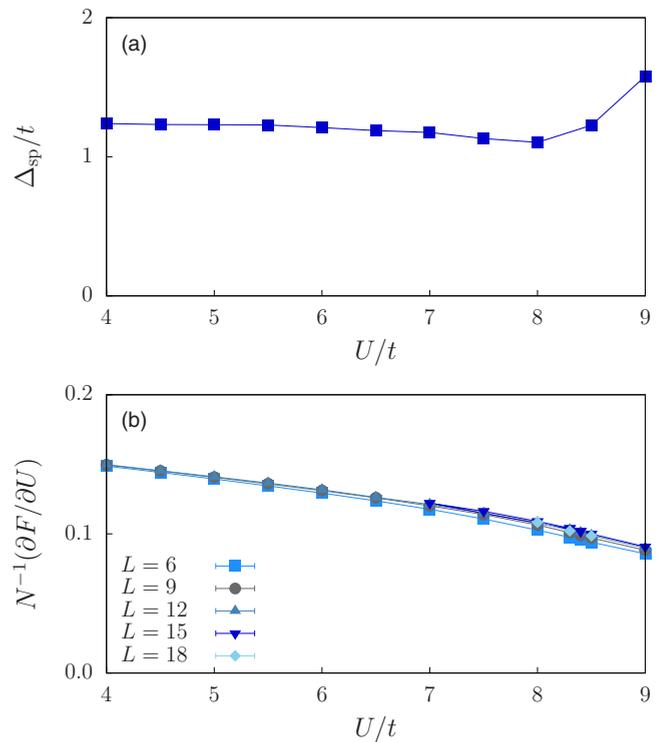
FIG. 7. (Color online) (a) Finite-size extrapolated single-particle gap. (b) Expectation value of the interaction term, corresponding to the derivative of the free energy with respect to U. Here, $\lambda/t = 0.2$, $\alpha = 1$.

at sufficiently large values of the spin-orbit coupling upon increasing the Hubbard interaction [13]. While the model for Na_2IrO_3 includes a Rashba spin-orbit term that does not conserve spin [12,13], mean-field calculations suggest that such an interaction is not essential for the existence of the QSH* phase, and that this phase could also exist in the KMH model [48]. Its absence in numerical results for the KMH model may therefore be due to the onset of magnetic order already at intermediate values of U/t. (Similar to the QSH phase, the QSH* phase relies on time-reversal symmetry, and can therefore not coexist with magnetism.) Because the onset of magnetic order is shifted to stronger interactions, the KMC model can in principle provide a more favorable setting to observe this exotic phase.

Because the QSH* phase is not adiabatically connected to the QSH phase of the KM model, we expect this phase to manifest itself in terms of an additional phase transition. While a closing of the single-particle gap is not generally necessary in correlated systems, we still expect such a transition to leave a signature in the evolution of the gap with increasing U. However, the results for the single-particle gap of the KMC model shown in Fig. 7(a) are qualitatively the same as for the KMH model, and can be reproduced at the mean-field level [30]. The single-particle gap remains nonzero throughout the QSH phase, and shows a single cusp at the critical point of the magnetic transition. Similarly, and as in the case of $\lambda = 0$, the free-energy derivative with respect to the interaction shows a continuous evolution as a function of U [see Fig. 7(b)]. Finally, because the QSH* phase is expected to be located

between the QSH and the MI phase, it would change the universality class of the magnetic transition, the latter being a QSH*-MI transition instead of a QSH-MI transition. The scaling collapse obtained with the 3D XY critical exponents in Fig. 6(c) hence contradicts the existence of an intermediate phase. Finally, the response to π fluxes could be used to measure the Z_2 topological invariant as a function of U [41].

V. CONCLUSIONS

We have studied the Kane-Mele model with long-range Coulomb interaction using an auxiliary-field quantum Monte Carlo method. The phase diagram shows the same phases and phase transitions as for the Kane-Mele-Hubbard model, namely, a semimetal, a quantum spin Hall phase, and an antiferromagnetic Mott insulator. Most notably, the magnetic transition is shifted to significantly larger onsite interactions (in addition to the nonlocal part) compared to a Hubbard interaction. This shift can be understood as originating from the competition between charge and spin order, with charge fluctuations being enhanced by the nonlocal interactions.

The phase transitions between the semimetal and the antiferromagnetic insulator in the absence of spin-orbit coupling, and between the quantum spin Hall insulator and the antiferromagnetic insulator in the presence of spin-orbit coupling, were

analyzed with regard to the critical behavior. In both cases, the critical exponents appear to be the same as for the Hubbard interaction, namely, those of the Gross-Neveu and the 3D XY universality classes, respectively. This observation agrees with analytical findings regarding the marginal irrelevance of the long-range interaction. Compared to the case of a Hubbard interaction, the problem with long-range interactions is more challenging. Consequently, the finite-size extrapolations and critical values are less accurate.

Finally, we did not find any evidence for additional phases. Our results suggest that apart from quantitative differences, the Hubbard repulsion captures the essential physics associated with strong correlations. Unfortunately, because of a minus-sign problem, our method cannot be applied to models with dominant nearest- or next-nearest-neighbor interactions which may support additional symmetry-breaking phases [3].

[1] K. S. Novoselov, A. K. Geim, S. V. Morozov, D. Jiang, M. I. Katsnelson, I. V. Grigorieva, S. V. Dubonos, and A. A. Firsov, Nature (London) **438**, 197 (2005).

[2] C. L. Kane and E. J. Mele, Phys. Rev. Lett. **95**, 226801 (2005).

[3] S. Raghu, X.-L. Qi, C. Honerkamp, and S.-C. Zhang, Phys. Rev. Lett. **100**, 156401 (2008).

[4] M. Daghofer and M. Hohenadler, Phys. Rev. B **89**, 035103 (2014).

[5] N. A. García-Martínez, A. G. Grushin, T. Neupert, B. Valenzuela, and E. V. Castro, Phys. Rev. B **88**, 245123 (2013).

[6] T. Đurić, N. Chancellor, and I. F. Herbut, Phys. Rev. B **89**, 165123 (2014).

[7] Z. Y. Meng, T. C. Lang, S. Wessel, F. F. Assaad, and A. Muramatsu, Nature (London) **464**, 847 (2010).

[8] X. Chen, Z.-C. Gu, Z.-X. Liu, and X.-G. Wen, Science **338**, 1604 (2012).

[9] S. Sorella, Y. Otsuka, and S. Yunoki, Sci. Rep. **2**, 992 (2012).

[10] F. F. Assaad and I. F. Herbut, Phys. Rev. X **3**, 031010 (2013).

[11] B. K. Clark, arXiv:1305.0278.

[12] A. Shitade, H. Katsura, J. Kunes, X.-L. Qi, S.-C. Zhang, and N. Nagaosa, Phys. Rev. Lett. **102**, 256403 (2009).

[13] A. Rüegg and G. A. Fiete, Phys. Rev. Lett. **108**, 046401 (2012).

[14] J. Hubbard, Proc. R. Soc. London **276**, 238 (1963).

[15] S. Sorella and E. Tosatti, Europhys. Lett. **19**, 699 (1992).

[16] T. Paiva, R. T. Scalettar, W. Zheng, R. R. P. Singh, and J. Oitmaa, Phys. Rev. B **72**, 085123 (2005).

[17] M. Hohenadler, T. C. Lang, and F. F. Assaad, Phys. Rev. Lett. **106**, 100403 (2011).

[18] D. Zheng, G.-M. Zhang, and C. Wu, Phys. Rev. B **84**, 205121 (2011).

[19] S. Rachel and K. Le Hur, Phys. Rev. B **82**, 075106 (2010).

[20] M. Hohenadler and F. F. Assaad, J. Phys.: Condens. Matter **25**, 143201 (2013).

[21] A. H. Castro Neto, F. Guinea, N. M. R. Peres, K. S. Novoselov, and A. K. Geim, Rev. Mod. Phys. **81**, 109 (2009).

[22] P. R. Wallace, Phys. Rev. **71**, 622 (1947).

[23] I. F. Herbut, Phys. Rev. Lett. **97**, 146401 (2006).

[24] I. F. Herbut, V. Juričić, and O. Vafek, Phys. Rev. B **80**, 075432 (2009).

[25] L. Janssen and I. F. Herbut, Phys. Rev. B **89**, 205403 (2014).

[26] J. Gonzalez, F. Guinea, and M. A. H. Vozmediano, Nucl. Phys. B **424**, 595 (1994).

[27] J. González, F. Guinea, and M. A. H. Vozmediano, Phys. Rev. B **59**, R2474 (1999).

[28] D. C. Elias, R. V. Gorbachev, A. S. Mayorov, S. V. Morozov, A. A. Zhukov, P. Blake, L. A. Ponomarenko, I. V. Grigorieva, K. S. Novoselov, F. Guinea, and A. K. Geim, Nat. Phys. **7**, 701 (2011).

[29] V. Juričić, I. F. Herbut, and G. W. Semenoff, Phys. Rev. B **80**, 081405(R) (2009).

[30] M. Hohenadler, Z. Y. Meng, T. C. Lang, S. Wessel, A. Muramatsu, and F. F. Assaad, Phys. Rev. B **85**, 115132 (2012).

[31] J. E. Drut and T. A. Lähde, Phys. Rev. Lett. **102**, 026802 (2009).

[32] A. Sekine, T. Z. Nakano, Y. Araki, and K. Nomura, Phys. Rev. B **87**, 165142 (2013).

[33] Y. Araki and T. Kimura, Phys. Rev. B **87**, 205440 (2013).

[34] A. Sekine and K. Nomura, J. Phys. Soc. Jpn. **83**, 094710 (2014).

[35] A. Sekine and K. Nomura, arXiv:1405.6932.

[36] C. L. Kane and E. J. Mele, Phys. Rev. Lett. **95**, 146802 (2005).

[37] M. V. Ulybyshev, P. V. Buividovich, M. I. Katsnelson, and M. I. Polikarpov, Phys. Rev. Lett. **111**, 056801 (2013).

[38] R. T. Scalettar, D. J. Scalapino, R. L. Sugar, and D. Toussaint, Phys. Rev. B **36**, 8632 (1987).

[39] F. F. Assaad and H. G. Evertz, in *Computational Many Particle Physics*, Lecture Notes in Physics, Vol. 739, edited by H. Fehske, R. Schneider, and A. Weiße (Springer, Berlin, 2008), p. 277.

[40] M. Feldbacher and F. F. Assaad, Phys. Rev. B **63**, 073105 (2001).

[41] F. F. Assaad, M. Bercx, and M. Hohenadler, Phys. Rev. X **3**, 011015 (2013).

[42] F. F. Assaad and M. Hohenadler, inSIDE **11**, 22 (2013).

[43] I. F. Herbut, V. Juričić, and B. Roy, Phys. Rev. B **79**, 085116 (2009).

[44] S. Chandrasekharan and A. Li, Phys. Rev. D **88**, 021701 (2013).

[45] B. Roy, V. Juričić, and I. F. Herbut, Phys. Rev. B **87**, 041401 (2013).

[46] M. Schüler, M. Rösner, T. O. Wehling, A. I. Lichtenstein, and M. I. Katsnelson, Phys. Rev. Lett. **111**, 036601 (2013).

[47] M. Campostrini, M. Hasenbusch, A. Pelissetto, and E. Vicari, Phys. Rev. B **74**, 144506 (2006).

[48] G. Fiete (private communication).